Journal of Applied Physics ARTICLE pubs.aip.org/aip/jap

Ion irradiation-driven unit-cell expansion and strain accumulation behavior in magnesium oxide

Cite as: J. Appl. Phys. **139**, 095902 (2026); doi: 10.1063/5.0310580
Submitted: 3 November 2025 · Accepted: 21 January 2026 ·
Published Online: 5 March 2026

Eric C. O'Quinn,[1] David J. Sprouster,[2] Cale C. Overstreet,[1] Jacob Minnette,[1] M. Saima Haque,[2] Maria Eugenia Toimil-Molares,[3,4] Miguel L. Crespillo,[1,5] Maik K. Lang,[1] Lance L. Snead,[2] and Jason R. Trelewicz[2,6,7,a)]

AFFILIATIONS

[1]Department of Nuclear Engineering, University of Tennessee, Knoxville, Tennessee 37996, USA
[2]Department of Materials Science & Chemical Engineering, Stony Brook University, Stony Brook, New York 11784, USA
[3]GSI Helmholtzzentrum für Schwerionenforschung, Darmstadt 64291, Germany
[4]Technische Universität Darmstadt, Darmstadt 64287, Germany
[5]Centro de Micro-Análisis de Materiales (CMAM), Universidad Autónoma de Madrid, Madrid E-28049, Spain
[6]Institute for Advanced Computational Science, Stony Brook University, Stony Brook, New York 11794, USA
[7]Materials Science and Technology Division, Oak Ridge National Laboratory, Oak Ridge, Tennessee 37831, USA

[a)]**Author to whom correspondence should be addressed:** jason.trelewicz@stonybrook.edu

ABSTRACT

Ceramic oxides offer a range of advantageous characteristics for withstanding intense mixed radiation fields, and consequently, interest has grown in exploring their behavior for nuclear applications such as fuel matrices and waste forms. In this study, magnesium oxide (MgO) was irradiated with ions of varying species, energies, and fluences, and the resulting structural modifications were characterized using synchrotron-based x-ray diffraction (XRD) combined with grazing-incidence XRD. Across all irradiation conditions, unit-cell expansion was observed, increasing with fluence. The magnitude of expansion was most significant for ions that primarily lose energy through nuclear interactions and lowest for those dominated by electronic excitations, spanning nearly two orders of magnitude. Under highly ionizing conditions, lattice swelling was reduced, but microstrain accumulation was enhanced, suggesting that defects are more localized and contribute less to long-range structural changes. These findings reveal the distinct roles of nuclear and electronic energy loss in defect formation and provide mechanistic insight into radiation-induced modifications in MgO, with implications for the design of radiation-tolerant materials for advanced nuclear technologies. Finally, the framework we present—incorporating an irradiation matrix that spans both nuclear and electronic energy loss dominated regions, strengthened by advanced quantitative XRD characterization—is widely applicable to the study of defect physics in polycrystalline materials.

I. INTRODUCTION

Ceramics exhibit a range of excellent physical and chemical properties, making them essential for energy technologies requiring a specific function (e.g., dielectric properties) and/or the ability to withstand extreme environments. Ceramic oxides play a crucial role throughout the nuclear fuel cycle, serving as fuel forms (e.g., UO_2) and waste forms (e.g., pyrochlore-structured complex oxides or borosilicate glasses).[1–3] These technologies are operated under extreme conditions, including elevated temperatures, chemically reactive environments, and intense particle irradiation.[4] Understanding the mechanism by which harsh environments induce structural modifications in oxide materials is essential for the continued development and optimization of advanced nuclear energy systems.[5]

In the nuclear fuel cycle, actinides undergo radioactive decay and nuclear fission, generating energetic particles that modify the surrounding matrix—whether it be a fuel or waste form. Alpha decay is especially detrimental to waste form durability,[6] yielding:

(i) a heavy recoil nucleus (<1 keV/u) that travels ∼20 nm and (ii) an energetic helium nucleus ("alpha particle" with >1 MeV/u) that travels ∼20 μm, over three orders of magnitude further than the heavy recoil nucleus.[7,8] These two particles deposit energy via fundamentally different mechanisms. In case (i), the low-energy heavy recoil nucleus (for instance, 86 keV ^{235}U in the alpha decay of ^{239}Pu) directly displaces target atoms through ballistic collisions with nuclei. These energetic displaced nuclei themselves produce additional recoil nuclei, generating a *displacement cascade*. Although many displaced atoms recombine with their vacant sites, a fraction remains permanently displaced. In case (ii), alpha particles (e.g., with 5.2 MeV in the alpha decay of ^{239}Pu) transfer energy primarily through electronic excitation and ionization. These processes take place over femtoseconds, creating a state of warm dense matter[9,10] far-from-equilibrium. The promotion of valence electrons to the conduction band modifies the local potential energy landscape while the subsequent electron–hole recombination generates a *thermal spike*, which drives the material through ordinarily unavailable structural pathways, quenching in defects, crystalline-crystalline transformations,[11] or even amorphization. In many insulators, these structural modifications remain permanently within nanometric cylindrical damage zones (*ion tracks*), concentric to the ion path.[12] Electronic interactions are also the mechanism by which large atomic fragments (∼1 MeV/u) generated from nuclear fission deposit most of their energy.[10]

Magnesium oxide (MgO) has been studied for over 60 years as a radiation-tolerant material[13–17] for inert matrix fuel applications[18,19] and fusion reactor environments[20–22] including recent work on its development as shielding materials.[23,24] Early studies investigating the response of MgO under irradiation focused on neutron bombardment,[17,25,26] revealing that MgO does not amorphize under directly displacing radiation conditions, like case (*i*) above. In fact, subsequent research has demonstrated that MgO remains crystalline at temperatures as low as 20 K,[22,27–29] with its critical amorphization temperature (T_c) often taken to be 0 K. Electron spin resonance experiments identified the primary radiation-induced point defects to be *F*-centers, oxygen vacancies occupied by single electrons.[17] Transmission electron microscopy studies further revealed interstitial dislocation loops.[25,26,30,31] Tench and Duck[15] irradiated MgO with 20 MeV protons and observed that the number of post-irradiation stabilized vacancies to be an order of magnitude lower than expected for primary knock-on damage, without even accounting for further displacements from damage cascades. These results indicate that vacancy production is inefficient, and that interstitial-vacancy recombination is highly effective in MgO, either during the initial athermal process or via subsequent interstitial diffusion. Supporting this, Zinkle and Snead[22] observed only dislocation loops and network dislocations in MgO exposed to low-energy ion irradiation, attributing this to high interstitial mobility and rapid recombination. Molecular and temperature-accelerated dynamics simulations conducted by Uberuaga *et al.*[18] revealed that collision cascades at 300 K produce interstitials and interstitial clusters, which diffuse quickly while vacancies and vacancy clusters remain sessile over century timescales, supporting prior experimental studies. Additional atomistic simulations of alpha-recoil-type collision cascades performed by Trachenko *et al.*[28] demonstrated that the vast majority of defects produced by alpha-recoil-type irradiation (40 keV U) recover within several picoseconds. They attributed this extraordinary resilience to lasting radiation-induced damage to the highly ionic nature of MgO; strong ionic bonds between Mg and O lead to a post-irradiation landscape dominated by electrostatic forces. This leads to fewer potential energy minima and a reduced ability to form disordered short-range networks,[28] unlike in covalently bonded systems.

MgO is also highly resistant to damage from electronic excitations and ionizations [as in case (ii) above]. It shows remarkable resilience to the photochemical effects of electron–hole recombination, unlike alkali halides such as LiF and NaCl, which share the same rock salt structure.[16] One of the earliest studies of MgO under ionizing radiation was conducted by Chen and Sibley,[14,16] who observed that exposure to electrons and gamma rays produced a 2.3 eV optical absorption band associated with V_1 centers, magnesium vacancies containing trapped holes. However, they found that this absorption band correlated strongly with impurity concentrations in MgO and was negligible compared to damage from elastic collisions in high-purity samples. MgO also exhibits weak electron–phonon coupling, resembling metals and semiconductors with its high electron and hole mobilities.[32] While energetic ions may excite electrons across the bandgap, charge neutralization occurs rapidly due to efficient electron–hole recombination. Consequently, the formation and trapping of holes or excitons, and their associated structural distortions, are unlikely, if not impossible, in bulk MgO.[33] By contrast, self-trapped excitons are common in other insulators such as SiO_2, and both excitons and holes readily self-trap in alkali halides.[34] Ionizing radiation can also generate peroxy radicals, defects composed of bound oxygen atom pairs. In close-packed oxides like MgO, the dense structure typically prevents the formation of these defects.[35] In contrast, peroxy radicals form more readily in materials such as SiO_2 or CeO_2, where greater structural flexibility permits their accommodation.[36]

While ionizing radiation often generates damage in insulators, it can also promote defect recovery by enhancing point defect mobility and enabling recombination through electronic processes.[13,37,38]For example, electron irradiation of MgO at 4 K produced *F*-centers at low fluences, but at higher fluences, defect concentrations saturated due to long-range, uncorrelated interstitial-vacancy recombination,[38] suggesting that oxygen interstitials can diffuse even at cryogenic temperatures with minimal thermal activation. This diffusion behavior can be explained by the Bourgoin–Corbett mechanism,[39] in which periodic modulation of the oxygen charge state drives defect mobility. A site that is stable for a neutral oxygen atom becomes an energetic saddle point for an oxygen anion and vice versa.[38]

Despite extensive studies on the structural effects of both ionizing and ballistic radiation in MgO,[22,28,35,38,40,41] understanding how radiation-induced defects contribute to strain accumulation and unit-cell expansion remains an open and important research challenge. Although MgO is often considered a simple model oxide, recent studies have revealed complex behavior at high temperatures and under far-from-equilibrium conditions, including differences in the defect accumulation behavior of vacancies and interstitials[18] as well as strongly correlated phonon behavior and breakdown of the phonon band theory.[42] This underscores the

TABLE I. Irradiation conditions used in this study.

Energy and ion species (MeV)	Velocity (c)	Flux (ions/cm^2 s)	Fluence (ions/cm^2)	Electronic ion energy loss at surface (keV/nm)	Nuclear ion energy loss at surface (keV/nm)
4 MeV Au[a]	0.007	$\leq 5 \times 10^8$	$4 \underline{\times} 10^{15}$, 7.8×10^{15}	3.601	3.045
198 MeV Xe	0.057	$\leq 5 \times 10^8$	8×10^{11}–8×10^{13}	23.770	0.081
946 MeV Au	0.101	$\leq 2 \times 10^9$	8×10^{11}–8×10^{13}	34.570	0.061
1.46 GeV Au[b]	0.125	$\leq 5 \times 10^8$	8×10^{12}	33.820	0.042

[a]Irradiation condition performed only on the fine-grained MgO samples.
[b]Follows the procedures described in O'Quinn *et al.*[45]

need to rigorously assess how MgO responds to extreme energy densities, such as those induced by ion irradiation. Such insights are essential for designing materials for advanced nuclear systems, where long-range structural changes arise from complex defect dynamics. In this study, we probe irradiation-induced structural modifications in MgO using energetic ion beams from multiple accelerator facilities, combined with synchrotron x-ray diffraction. To isolate the role of nuclear interactions, we irradiated samples with 4 MeV Au ions, which deposit a high fraction of their energy via elastic collisions, like alpha-recoil nuclei in waste forms. To examine the effects of electronic excitation and ionization, additional samples were exposed to 198 MeV Xe, 946 MeV Au, and 1.46 GeV Au ions.

II. METHODOLOGY

A. Sample synthesis

Fabrication of monolithic MgO compacts was accomplished using a SinterLand LABOX- 3010KF field assisted sintering system. Two MgO powder feedstocks with different average particle size (APS) distributions were used to produce coarse-grained (American Elements, 99.99% purity, APS $\leq 10\,\mu$m, average coherent domain size 145 nm) and fine-grained (US Research Nanomaterials, 99.95% purity, APS 50 nm, average coherent domain size 45 nm) MgO samples. Each MgO powder was blended with 1 wt. % LiF powder (Sigma-Aldrich, 99.98% purity, APS $< 100\,\mu$m) using a speed mixer (FlackTek DAC-1100). LiF serves as a fugitive sintering aid to suppress the sintering temperatures through diffusion of Li to interfaces and surfaces, where charge balance necessitates the formation of excess oxygen vacancies and leads to enhanced surface diffusion.[43] The LiF completely decomposes during the sintering process such that the resulting MgO compact is free of impurity phases.[44]

Green bodies were produced from the respective powder mixtures through cold pressing into a 25 mm hardened steel die at a pressure of 100 MPa for 5 min. The green bodies were subsequently loaded into a 25 mm graphite die with graphite foil liners and wrapped with carbon felt to reduce thermal losses during the heating cycle. The graphite die assembly was heated to 1100 °C using a rate of 50 °C/min, where it was held for 10 min followed by controlled cooling at 50 °C/min to 400 °C. The slow heating rate was selected to minimize the effective temperature gradients that form within the green body during heating and cooling. A uniaxial pressure of 10 MPa was applied to facilitate the densification while sustaining electrical contact during displacement of the die assembly. The chamber was maintained under vacuum during sintering with pressures not exceeding 10 Pa.

B. Irradiation experiments

Samples were exposed to a variety of ion species, energies, flux, and fluences described in Table I. Coarse- and fine-grained MgO–LiF samples were ground into powders and pressed into custom-milled chambers drilled into 25 μm thick molybdenum foil strips adhered by the ends to a rectangular aluminum bracket. Ten such brackets were prepared identically and each exposed to a broadly defocused beam of 946 MeV ^{197}Au ions at the M-branch of the GSI Helmholtz Centre's universal linear accelerator (UNILAC) in Darmstadt, Germany. Each bracket was irradiated under identical conditions at room temperature to a different fluence ranging from 5×10^{11} ions/cm^2 on the first bracket to 8×10^{13} ions/cm^2 on the last. Initial flux conditions are provided in Table I with the 5×10^8 ions/cm^2 s selected based on prior 1.46 GeV Au irradiations described in O'Quinn *et al.*;[45] the other irradiations employed the same initial flux condition to limit sample heating except for the 946 MeV Au, which had a slightly higher initial flux of 2×10^9 ions/cm^2 s. According to calculations performed with the SRIM software package,[46] the ions penetrated the sample fully and deposited 33(2) keV/nm along their path (Fig. 1), almost exclusively in the form of electronic excitations and ionizations. For this condition, nuclear interactions accounted for less than 0.4% of all energy transfer at all penetration depths. More details on this experimental setup can be found elsewhere.[47–49]

Using an identical sample holder setup, an additional series of coarse- and fine-grained samples were exposed to a broadly defocused beam of 198 MeV ^{131}Xe ions at the DC-60 cyclotron at the Astana Branch of the Institute of Nuclear Physics in Kazakhstan. These ions also fully penetrated the samples (Fig. 1), depositing 20(3) keV/nm along their path with nuclear interactions accounting for, at most, 2% of energy transfer at all penetration depths. Coarse- and fine-grained MgO samples were also exposed to 1.46 GeV ^{197}AU ions at the X0 beamline of the GSI Helmholtz Center for Heavy Ion Research in Darmstadt, Germany. For this condition, the powders were pressed into 10 mm diameter cylindrical indentations milled into aluminum plates. The mass of samples prepared in each chamber was determined by the thickness through which the ions would homogeneously deposit energy through electronic interactions [34.4(3) keV/nm with nuclear interactions accounting for ~0.1% of the energy transfer]. The holders were then mounted in a 3×3 grid on a thick aluminum plate

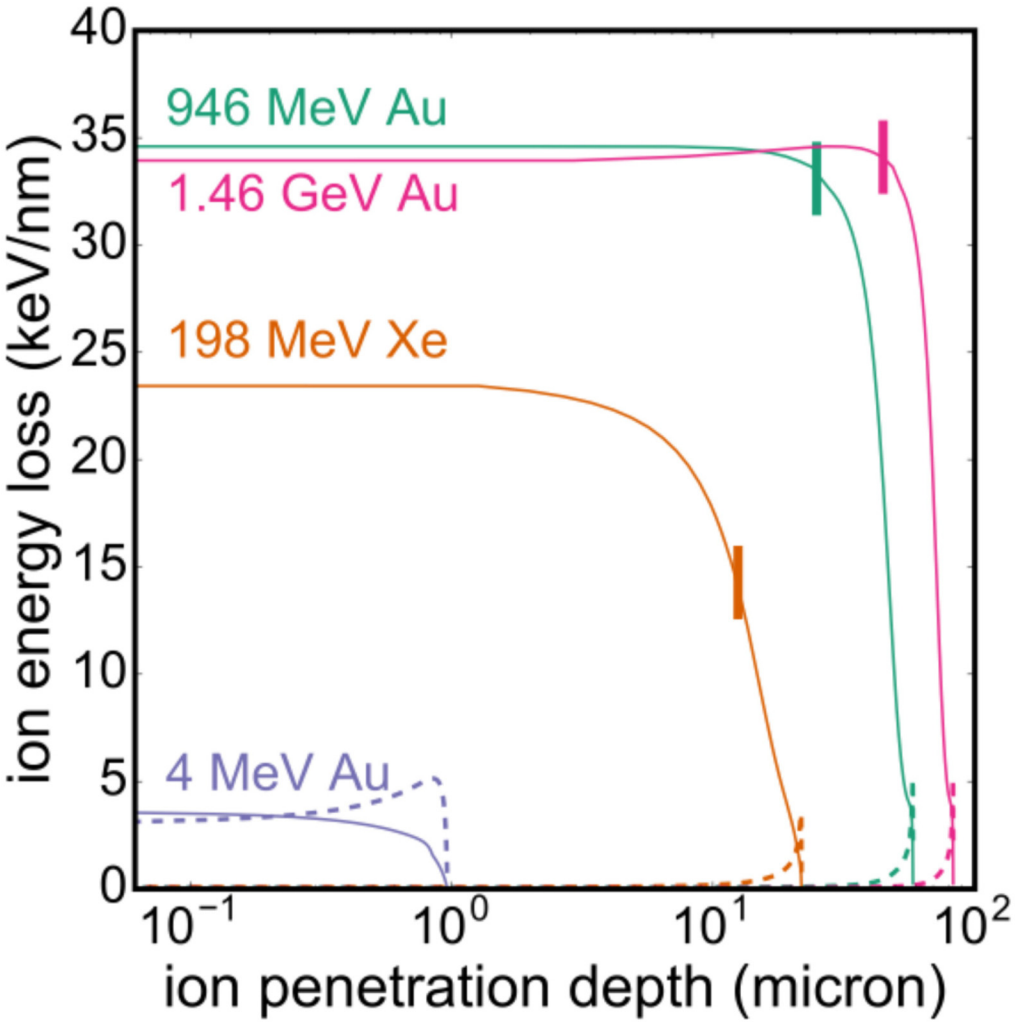

FIG. 1. Energy loss profiles of the four ions chosen for this study. The magnitude of energy loss through electronic interactions is shown as solid lines, while dashed lines denote energy loss through nuclear interactions. The thick vertical lines that intersect the data sets corresponding to 1.46 GeV Au, 946 MeV Au, and 198 MeV Xe indicate the sample thickness that was exposed to the ion beam.

and simultaneously irradiated with a broadly defocused beam to a single fluence of 8×10^{12} ions/cm^2. Finally, a 1 mm thick pellet of fine-grained MgO-LiF was partially covered with 50 μm thick steel foil and irradiated with a beam of 4 MeV ^{197}AU ions at the Centro de Micro-Análisis de Materiales (CMAM) in Madrid, Spain. The sample was exposed to a fluence of 7.8×10^{15} ions/cm^2, which corresponds to 12 displacements per atom (dpa). In contrast with the irradiation conditions described above, nuclear interactions play a significant role in the energy loss profile (Fig. 1) of 4 MeV Au ions.

C. X-ray diffraction

Samples that were irradiated in molybdenum chambers to a series of fluences (946 MeV Au and 198 MeV Xe) were characterized with synchrotron x-ray diffraction (XRD) at the 16-BM-D beamline (HPCAT sector) of the Advanced Photon Source at Argonne National Laboratory. Angle-dispersive XRD was performed using a monochromatic beam of 30.000 keV (0.413 28 Å) x rays in the Debye–Scherrer (transmission) geometry with a 5×4 μm beam spot and a sample-to-detector distance of 220 mm. A Pilatus3 X CdTe 1 M detector image plate detector recorded the Debye rings with a collection time of 180 s. Subsequent two-dimensional diffraction images were integrated into one-dimensional x-ray diffraction patterns using Dioptas[50] covering a reciprocal space range up to 7.87 Å^{-1}.

For samples irradiated with 1.46 GeV Au ions, x-ray diffraction experiments were performed at the National Synchrotron Light Source-II (NSLS-II) at Brookhaven National Laboratory using

beamline 28-ID-1 (Pair Distribution Function beamline).[51] The samples were removed from their aluminum chambers with a blunt tip needle and placed in a 0.6 mm diameter Kapton capillary with a foam seal at both ends. LaB_6 and CeO_2 calibration standards along with empty sample containers were collected to ensure correct sample-to-detector distance, and instrument contribution to the XRD patterns were effectively captured during analysis. Powder x-ray diffraction data was acquired with an exposure time of 60 s under a monochromatic beam of 74.465 keV (0.1665 Å) x rays and a sample-to-detector distance of 1050 mm. Two-dimensional diffractograms were produced using a PerkinElmer XRD 1621 detector and subsequently integrated into one-dimensional patterns using Dioptas[50] over a reciprocal space range up to 10.18 $Å^{-1}$.

Grazing-incidence x-day diffraction (GIXRD) was required to sample the shallow implantation damage surface for the 4 MeV Au (low-energy) irradiated specimens. These GIXRD patterns, optimized to enhance the irradiated surface (as shown below), yield XRD patterns that allow for the quantification of the average damage (i.e., irradiation depth-averaged) state. GIXRD measurements were conducted at Stony Brook University using a Bruker D8 Advance (Bruker, GMBH) with a Cu source ($K\alpha1 = 1.5406$ Å, $K\alpha2 = 1.5444$ Å) operating at a voltage of 40 kV and a current of 40 mA. After positioning and alignment of the specimen within the incident x-ray beam (and correcting for any specimen height/tip/tilt corrections), the samples were subsequently positioned with a 1-degree glancing angle (Omega, ω), and GIXRD patterns were collected from $Q = 2.452\,80$ to $5.243\,09$ $Å^{-1}$ in the Bragg–Brentano (reflection) geometry. Patterns were refined in TOPAS (Bruker) to quantify the unit-cell parameters of the irradiated surfaces. An unirradiated MgO GIXRD pattern was collected as a reference.

All diffraction patterns were analyzed using Rietveld refinement and the Williamson–Hall (W–H) method. Refinements were performed with GSAS-II[52] using a *Fm*-3*m* rock salt model (Wyckoff sites 4*a* and 4*b* occupied by Mg and O, respectively) with six variable parameters: the global scale factor, unit-cell parameter, heterogeneous microstrain, coherent domain size, and two isotropic atomic displacement parameters (Mg and O). However, the coherent domain size and heterogeneous microstrain were more accurately determined through the conventional W–H approach. Eight MgO diffraction peaks (111, 200, 220, 311, 222, 400, 331, and 420) between $Q = 2.5$–6.7 $Å^{-1}$ were selected for each data set and fit with pseudo-Voigt peak profiles [linear combination of Gaussian and Lorentzian profiles[53] in the Fityk program[54] to extract their peak positions (θ) and widths [$\beta_{sample} = (\beta^2_{total} - \beta^2_{instrument})^{1/2}$]. We note that the XRD-based microstrain increases with increasing density of two-dimensional defects, such as dislocations, grain boundaries, stacking faults, and defect clusters, that effectively cause nonuniform lattice distortions within crystallites.[55,56] Similarly, the coherent grain size from XRD is different from the grain size measured by scanning electron microscopy (SEM). While microscopy-based techniques resolve morphological grains defined by high-angle grain boundaries, XRD is sensitive to the internal crystalline coherence of the material. As such, a single grain observed by SEM may contain multiple coherently diffracting domains separated by low-angle boundaries, dislocation networks, or internal strain gradients, each of which limits diffraction coherence and reduces the apparent XRD coherent grain size.

III. RESULTS

Synchrotron XRD patterns for the 946 MeV Au irradiated samples shown in Fig. 2 indicate that the coarse- and fine-grained MgO samples are consistent with the rock salt structure (face-centered cubic space group 225 *Fm*-3*m*), as expected. There is another set of reflections present in the XRD pattern that arises from the molybdenum sample chamber (space group 229 *Im*-3*m*, $a \sim 3.147$ Å, Mo at Wyckoff site 2*a*) in which the sample was exposed to the x-ray beam. Diffraction peaks in the pattern of the coarse-grained sample are generally narrower than those in the fine-grained sample, consistent with either larger coherent domain sizes,[57] reduced heterogeneous strain, or a combination thereof. The most apparent effect of increasing radiation fluence is diffraction peak broadening in Fig. 2, particularly at higher scattering vectors [for example, the (420) peak at $Q \sim 6.7$ $Å^{-1}$]. No other effects such as a change in the distribution of diffraction peaks (indicating phase transformations) or the elimination of diffraction peaks accompanied by an increase in diffuse background signal (indicating amorphization) are observed.

Quantitative analysis of the most intense (200) peak shown was performed using pseudo-Voigt fitting. In the coarse-grained sample with the patterns shown in Fig. 3(a), the (200) peak shifted to smaller *Q*-values with increasing fluence, from 2.983 38(2) $Å^{-1}$ before irradiation to 2.982 37(8) $Å^{-1}$ after 8×10^{13} ions/cm^2. Concurrently, the full width at half maximum (FWHM) increases from 0.006 34(2) to 0.011 63(10) $Å^{-1}$. These trends reflect unit-cell expansion accompanied by either microstrain accumulation, reduced coherent domain size, or both. In the fine-grained sample with the patterns shown in Fig. 3(b), the (200) peak initially shifted to higher *Q*-values, from 2.982 45(3) to 2.982 87(12) $Å^{-1}$ at 8×10^{12} ions/cm^2, before shifting to lower values at higher fluences, reaching 2.980 23(3) $Å^{-1}$ after 8×10^{13} ions/cm^2. Peak broadening increased throughout, with FWHM increasing from 0.0168(1) $Å^{-1}$ before irradiation to 0.0362(2) $Å^{-1}$ at the highest fluence. Therefore, while peak broadening trends were similar in both samples, the fine-grained sample exhibited an initial unit-cell contraction followed by expansion at higher fluences. Rietveld refinements were used to quantify the change in lattice parameter, which is shown in Fig. 3(c) as a function of irradiation fluence. Prior to irradiation, the unit-cell parameters were determined to be 4.212 09(3) Å and 4.213 35(7) Å for the coarse- and fine-grained samples, respectively, closely matching reported values for MgO under ambient conditions.[58,59] In the coarse-grained sample, the unit cell expanded by approximately 0.02% at the lowest evaluated fluence (5×10^{11} ions/cm^2). No clear trend was observed with further increases in fluence, with the total change reaching only ~0.027% at the highest fluence of 8×10^{13} ions/cm^2. In contrast, the fine-grained sample initially exhibited a slight contraction of ~0.01% before expanding at higher fluences. At 8×10^{13} ions/cm^2, the unit-cell volume stabilized at an overall increase of approximately 0.06%.

In the samples irradiated with 198 MeV ^{131}Xe ions, XRD analysis confirmed phase purity in both coarse- and fine-grained MgO samples with reflections from only the rock salt MgO phase and the molybdenum sample chamber observed in the patterns shown in Fig. 4. No significant differences in diffraction peak widths were observed prior to irradiation. Upon irradiation, diffraction peaks in both samples broaden and shift to smaller *Q*-values as evidenced in

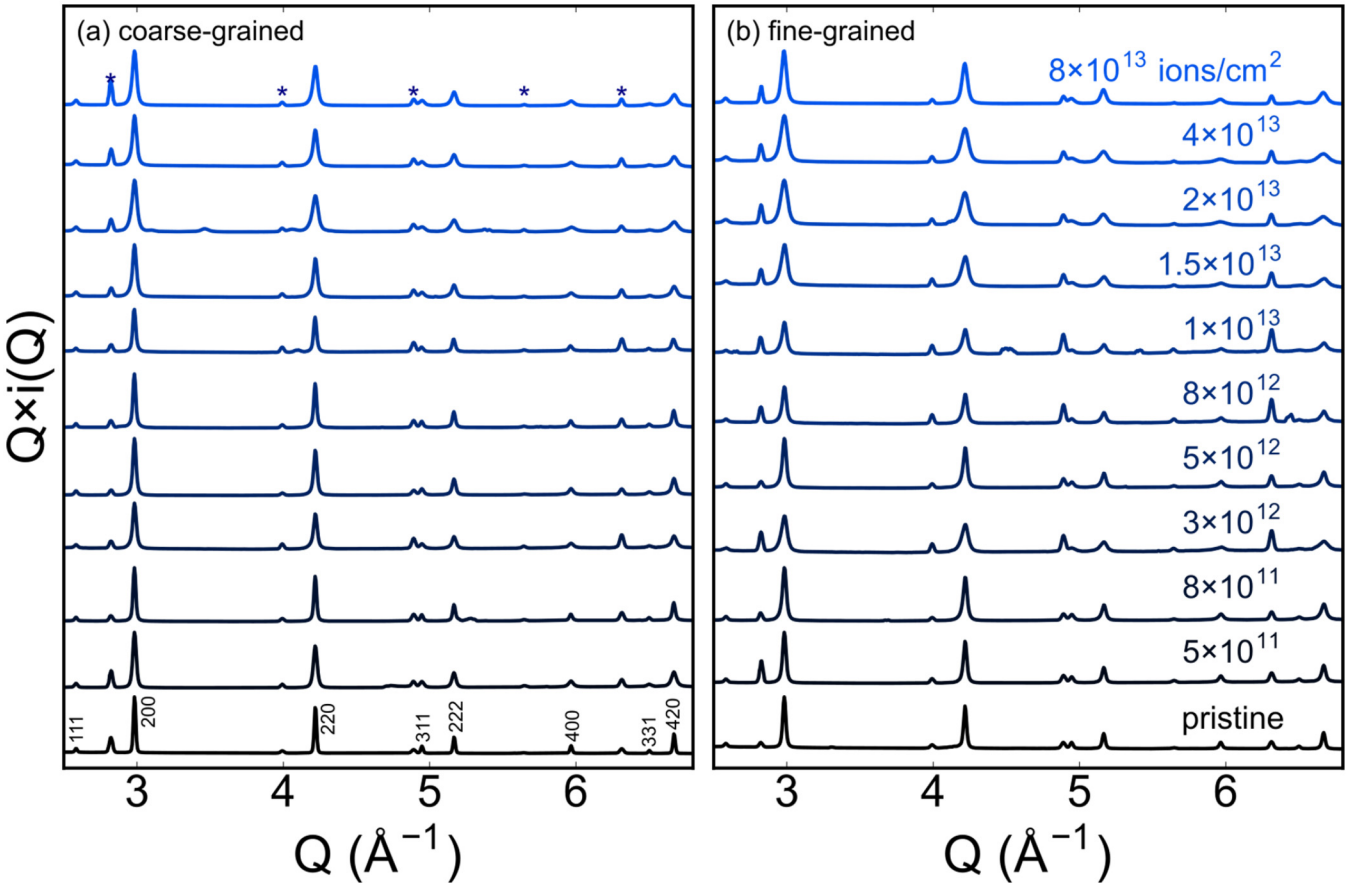

FIG. 2. X-ray diffraction patterns of (a) coarse- and (b) fine-grained MgO before and after exposure to indexed fluences of 946 MeV Au ions. The pattern is scaled with Q, the scattering vector, to offset the damping effect of the x-ray form factor. The asterisks in (a) denote peaks arising from the Mo sample chamber, which are also present in (b).

Figs. 5(a) and 5(b), indicating unit-cell expansion accompanied by increased microstrain, reduced coherent domain size, or a combination thereof.

Rietveld refinement of diffraction patterns revealed that exposure to the 198 MeV Xe ions produced unit-cell expansion in both the coarse- and fine-grained MgO samples in Fig. 5(c). Both samples, prior to irradiation, have nearly identical unit-cell parameters, 4.211 89(12) Å and 4.211 92(8) Å, respectively. At low fluences, unit-cell expansion is approximately linear with fluence. At higher fluences, the trend becomes sublinear and eventually saturates at an expansion of 0.07%–0.08%. The magnitude of lattice swelling under 198 MeV Xe irradiation therefore exceeded that observed for 946 MeV Au exposure, consistent with a direct impact mechanism,[60] where each ion produces a cylindrical damage zone that contributes to unit-cell swelling. At higher fluences, these zones accumulate and eventually overlap, leading to saturation. The direct impact model is given by the relation

$$\Delta a(\phi) = \Delta a_s[1 - \exp(-\sigma\phi)], \quad (1)$$

where a_0 is the unit-cell parameter prior to irradiation, $\Delta a(\phi)$ is the change in unit cell after exposure to a given fluence, ϕ, Δa_s is the unit-cell parameter change in the saturation regime, and σ is the damage area per ion. For a cylindrical geometry, the fitted damage cross sections, 17(3) nm^2 for fine- and 19(2) nm^2 for coarse-grained MgO, correspond to damage zone diameters of 4.7(4) nm and 4.9 (2) nm, respectively.

XRD patterns for coarse- and fine-grained MgO samples irradiated with a single fluence of 1.46 GeV Au ions (8×10^{12} ions/cm^2) are shown in Fig. 6 for the pristine and irradiated samples. The results are broadly consistent with those observed under lower energy irradiation, with one notable exception. All Bragg peaks are retained, with no change in their positions or distribution, indicating neither amorphization nor phase transformation. Both samples exhibit peak broadening following irradiation; however, the absence of peak shifts indicates minimal change in the unit-cell dimensions. Rietveld refinement confirmed this result, revealing a unit-cell expansion of 0.0081(5)% in coarse-grained MgO and 0.0041(1)% in the fine-grained sample. These values are approximately an

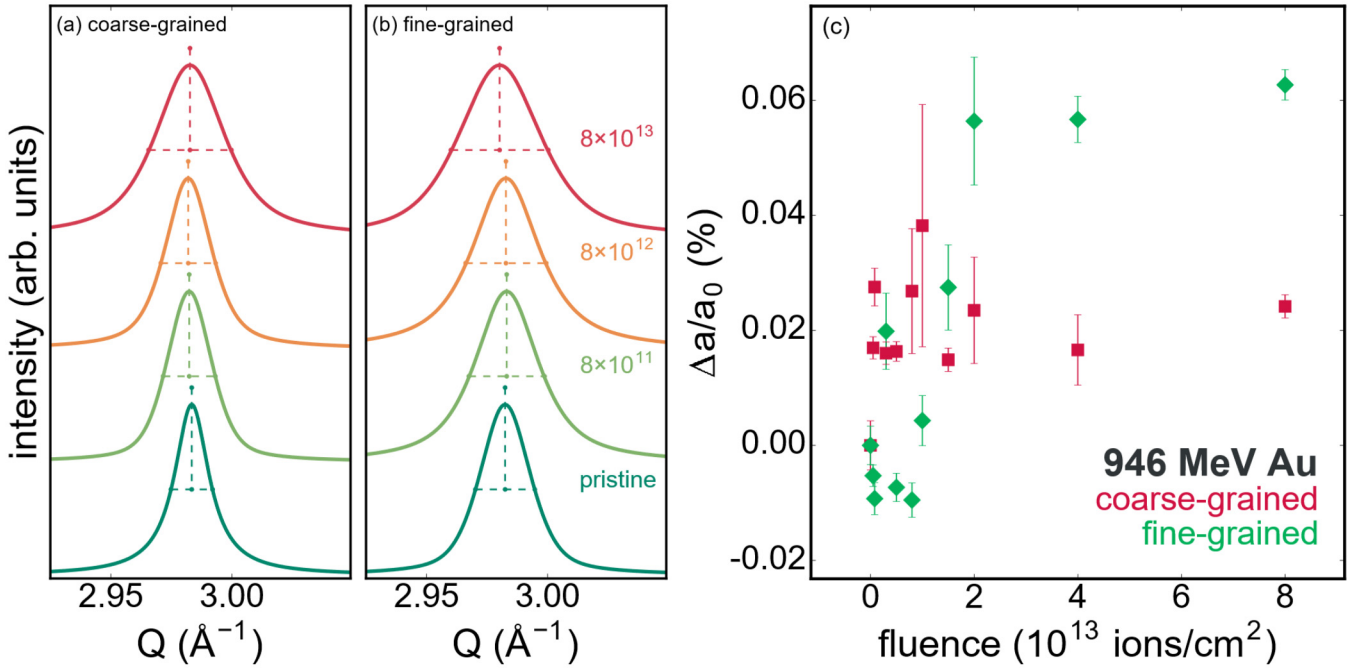

FIG. 3. Enlarged view of pseudo-Voigt fits to the (200) XRD peak in the (a) coarse- and (b) fine-grained MgO samples before and after exposure to indexed fluences of 946 MeV Au to display peak shift (dashed vertical lines) and broadening (dashed horizontal lines). (c) Unit-cell change induced by 946 MeV Au ions as determined by a Rietveld refinement. Uncertainties in (c) correspond to propagation of uncertainties arising from (i) the Rietveld refinement of each pattern and (ii) the consideration of multiple patterns for each fluence.

order of magnitude smaller than the lattice swelling observed under 198 MeV Xe irradiation.

The final set of irradiations employed 4 MeV Au ions on the fine-grained MgO to two fluences of 4.0×10^{15} and 7.8×10^{15} ions/cm^2, corresponding to 6 and 12 displacements per atom (dpa), respectively. Because the damage region is more localized to the surface, GIXRD was employed to measure changes in the irradiated surface layer post-ion exposure with the pattern for the sample exposed to 7.8×10^{15} ions/cm^2 shown in Fig. 7(a). Patterns from the irradiated surface and underlying bulk are overlaid in Fig. 7(b) for comparison. The surface layer exhibits clear peak shifts to lower scattering angles, consistent with unit-cell expansion. The refined unit cell expands by 0.3773(4)% after irradiation to 4.0×10^{15} ions/cm^2 and by 0.3640(3)% after 7.8×10^{15} ions/cm^2. These values are approximately five times greater than those observed for high-energy ion irradiation yet are similar across the two dose levels. These results suggest that at the 4 MeV Au fluences used here, lattice swelling reaches a saturation point. The higher fluence (7.8×10^{15} ions/cm^2) appears sufficient to induce overlapping cascades and steady-state defect production and recovery.

To quantify the fluence dependence of peak broadening and separate contributions from microstrain and coherent domain size reduction, a W–H analysis was applied to samples irradiated across multiple fluences from the 946 MeV Au and 198 MeV Xe ion irradiation experiments. Figure 8(a) shows a representative example of this analysis for the coarse-grained sample irradiated with 946 MeV Au ions. Both the slope and y-intercept increase with fluence, indicating a rise in microstrain and concomitant reduction in coherent domain size. The coherent domain size, D, and microstrain, ε, were extracted using the following relation:

$$\beta_{sample} \cos\theta = \epsilon(4 \sin\theta) + \frac{0.9\lambda}{D}. \quad (2)$$

Prior to irradiation, both coarse-grained samples exhibited comparable coherent domain sizes with some sample-to-sample variation. Irradiation with 946 MeV Au ions reduced the domain size of the coarse-grained sample in Fig. 8(b) followed by saturation at approximately 35 nm with increasing fluence. The fine-grained sample also exhibited a reduction in domain size, though with a smaller overall change than the coarse-grained counterpart. The fine grain coherent domain size stabilized near 20 nm across the full range of fluences studied. Saturation was also observed during irradiation with 198 MeV Xe ions in Fig. 8(d) but with a subtle increase relative to the pristine samples at fluences of $<2 \times 10^{13}$ ions/cm^2.

Heterogeneous microstrain values were extracted from the slopes of the W–H plots shown in Fig. 8(a). For 946 MeV Au ion irradiation in Fig. 8(c), microstrain in both the coarse- and fine-grained samples increased by more than an order of magnitude from initial values of 0.026(2)% and 0.035(14)%, respectively. Microstrain peaks at over 0.3% in both samples at

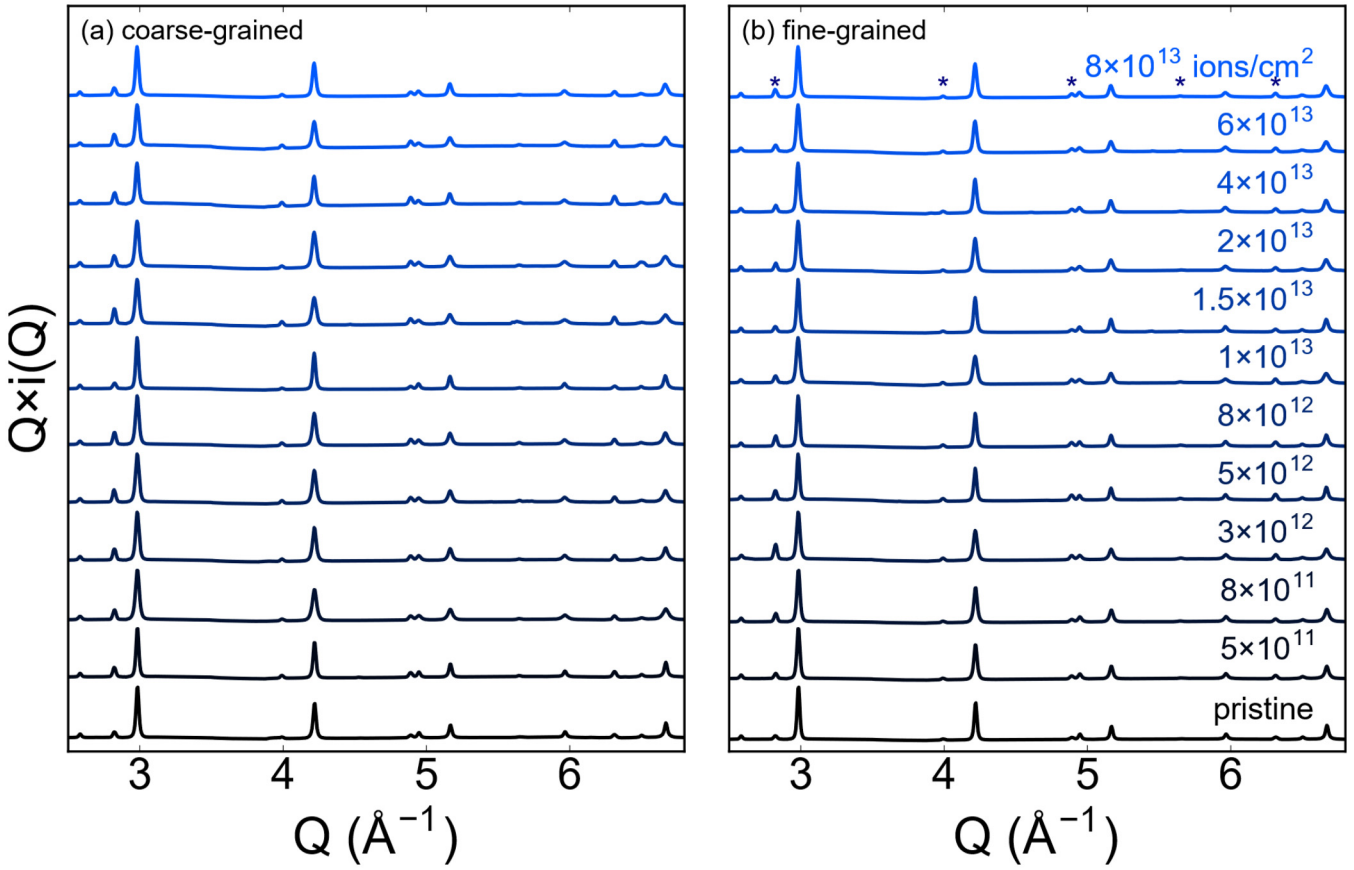

FIG. 4. X-ray diffraction patterns of (a) coarse- and (b) fine-grained MgO before exposure to indexed fluences of 198 MeV Xe ions. The pattern is scaled with Q, the scattering vector, to offset the effect of the x-ray form factor. The asterisks in (a) denote peaks arising from the Mo sample chamber, which are also present in (b).

2×10^{13} ions/cm^2, followed by a slight decrease to approximately 0.2% at the highest fluence evaluated. This initial linear increase, followed by sublinear growth and eventual saturation, is consistent with the direct impact model [Eq. (2)]. Fitting this model to the microstrain data yields interaction damage diameters of 2.6(6) nm for the coarse-grained sample and 3.6(7) nm for the fine-grained sample. Although these samples were only exposed to a single fluence of 1.46 GeV Au ions (8×10^{12} ions/cm^2), the resulting microstrain values—0.15(1)% and 0.29(3)%, respectively—are consistent with those measured in samples irradiated with 946 MeV Au ions at similar fluences. Irradiation by 198 MeV Xe ions produced a more subtle increase and saturation threshold in the microstrain shown in Fig. 8(d), consistent with coherent domain size evolution under these conditions.

IV. DISCUSSION

The comprehensive XRD analysis presented herein confirmed that MgO exhibits unit-cell expansion under all irradiation conditions evaluated, regardless of whether damage is driven primarily by electronic excitation and ionization (198 MeV Xe, 946 MeV Au, and 1.46 GeV Au) or by elastic collisions and atomic displacements (4 MeV Au), with results compiled in Table II. The largest expansion was observed following exposure to 4 MeV Au ions, whereas the smallest increase was measured after 1.46 GeV Au ion irradiation. Across all irradiation types, the extent of lattice swelling appears inversely correlated with ion energy. However, this trend alone obscures the underlying mechanisms of ion–matter interactions. High-energy ions primarily deposit energy through Coulomb interactions with the electronic subsystem, while low-energy ions lose energy mainly via elastic collisions with atomic nuclei. By selecting ions that span this spectrum, we varied the relative contributions of electronic and nuclear stopping, enabling us to probe their individual effects on structural modification in MgO. Shown in Fig. 9(a) is the relative contribution of nuclear interactions to ion energy loss with each ion type and energy matched on the various curves for Au and Xe. The maximum unit-cell expansion under each condition is plotted as a function of this nuclear stopping fraction (S_n/S_{total}) in Fig. 9(b) and reveals a direct correlation: greater lattice swelling corresponds to a

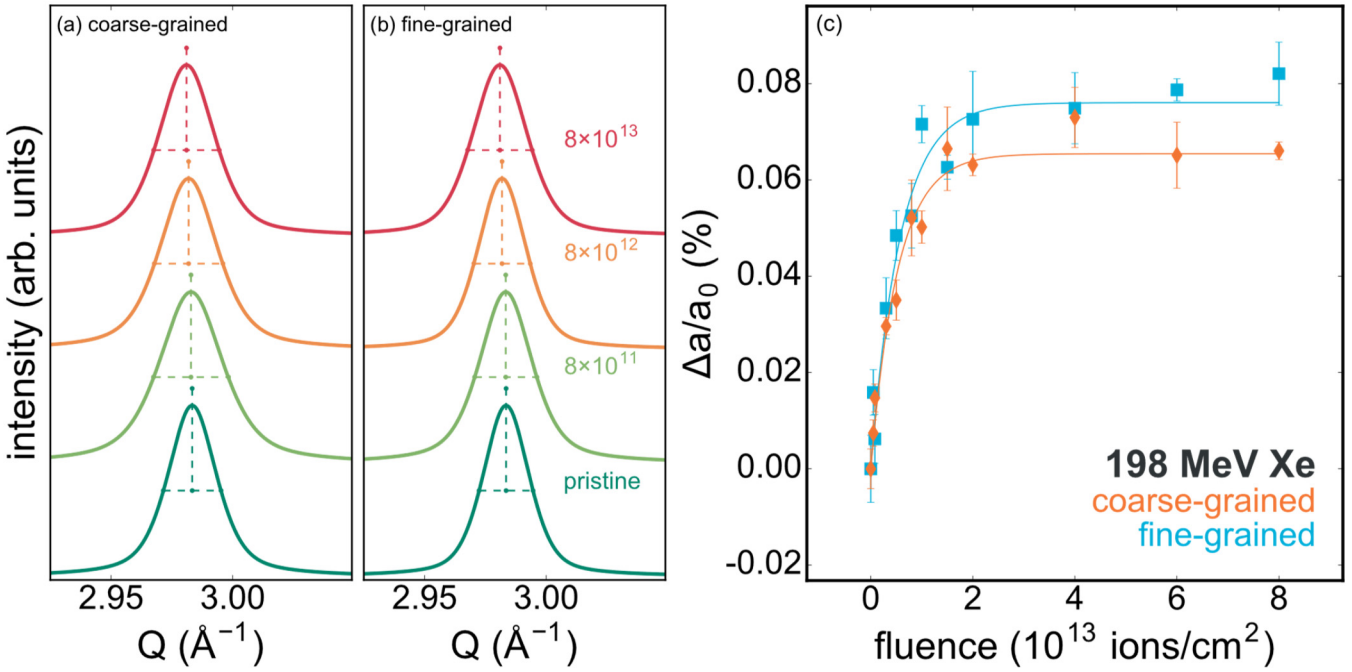

FIG. 5. Enlarged view of pseudo-Voigt fits to the (200) x-ray diffraction peak in the (a) coarse- and (b) fine-grained MgO samples before and after exposure to indexed fluences of 198 MeV Xe to display peak shift (dashed vertical lines) and broadening (dashed horizontal lines). (c) Unit-cell change induced in coarse- and fine-grained MgO by 198 MeV Xe ions as determined by Rietveld refinement of XRD patterns. Uncertainties in (c) correspond to the propagation of uncertainties arising from (i) the Rietveld refinement of each pattern and (ii) the consideration of multiple patterns for each fluence. Lines in (c) are the fit of Eq. (2) to the data.

higher fraction of energy deposited through nuclear interactions. This indicates that elastic collisions with nuclei, rather than electronic excitation, are the dominant driver of radiation-induced lattice swelling in MgO.

In ion irradiation regimes dominated by intense electronic ionizations and excitations, another mechanism may influence the magnitude of unit-cell expansion. Although the transfer of energy from ions to matter depends nonlinearly on ion energy, the spatial distribution of that energy is strongly affected by ion velocity. Specifically, the range of liberated δ-electrons increases with ion velocity, dispersing energy over a larger volume and thereby reducing the local energy density. As a result, higher velocity ions may induce less structural modification despite higher absolute energies. This phenomenon, often referred to as the "velocity effect,"[61,62] can be approximated by scaling the electronic stopping power (dE/dx) by the ion velocity β. When applied to our irradiations (Table I), it is clear that 198 MeV Xe induces the highest energy density, followed by 946 MeV Au, with 1.46 GeV Au producing the lowest. This trend aligns with our observed lattice swelling behavior, supporting the idea that local energy density, not total deposited energy, may also contribute to the structural modification trends observed within this regime.

The comparison between coarse- and fine-grained MgO reveals subtle differences in both unit-cell expansion and microstrain accumulation under identical irradiation conditions. In general, the fine-grained material exhibits larger maximum lattice expansions [Fig. 9(b)] and lower maximum microstrain (Fig. 10) than their coarse-grained counterparts. This behavior is generally attributed to the higher grain boundary density in the fine-grained MgO, which can modify the final defect microstructures post-irradiation.[63,64] The 1.46 GeV Au irradiations show subtle exceptions to this trend with the maximum lattice swelling in both fine and coarse MgO being identical, while the microstrain in the coarse-grained sample is lower than the fine-grained (as described above). These observations underscore that the irradiation response of MgO is not solely determined by defect production rates, but also by the microstructural length scales over which defects accumulate and relax. The distinction between nuclear and electronic stopping contributions in the fine- and coarse-grained MgO specimens is based on the nature and spatial distribution of the damage inferred from the XRD patterns. In the nuclear stopping-dominated region, collision cascades generate point defects, which manifest as larger apparent lattice parameter changes. At high fluence, these defects can cluster to form two-dimensional defects such as dislocation loops and clusters. In contrast, we observe that electronic stopping-dominated irradiation introduces localized disorder leading to increased microstrain without a proportional increase in average lattice parameter and

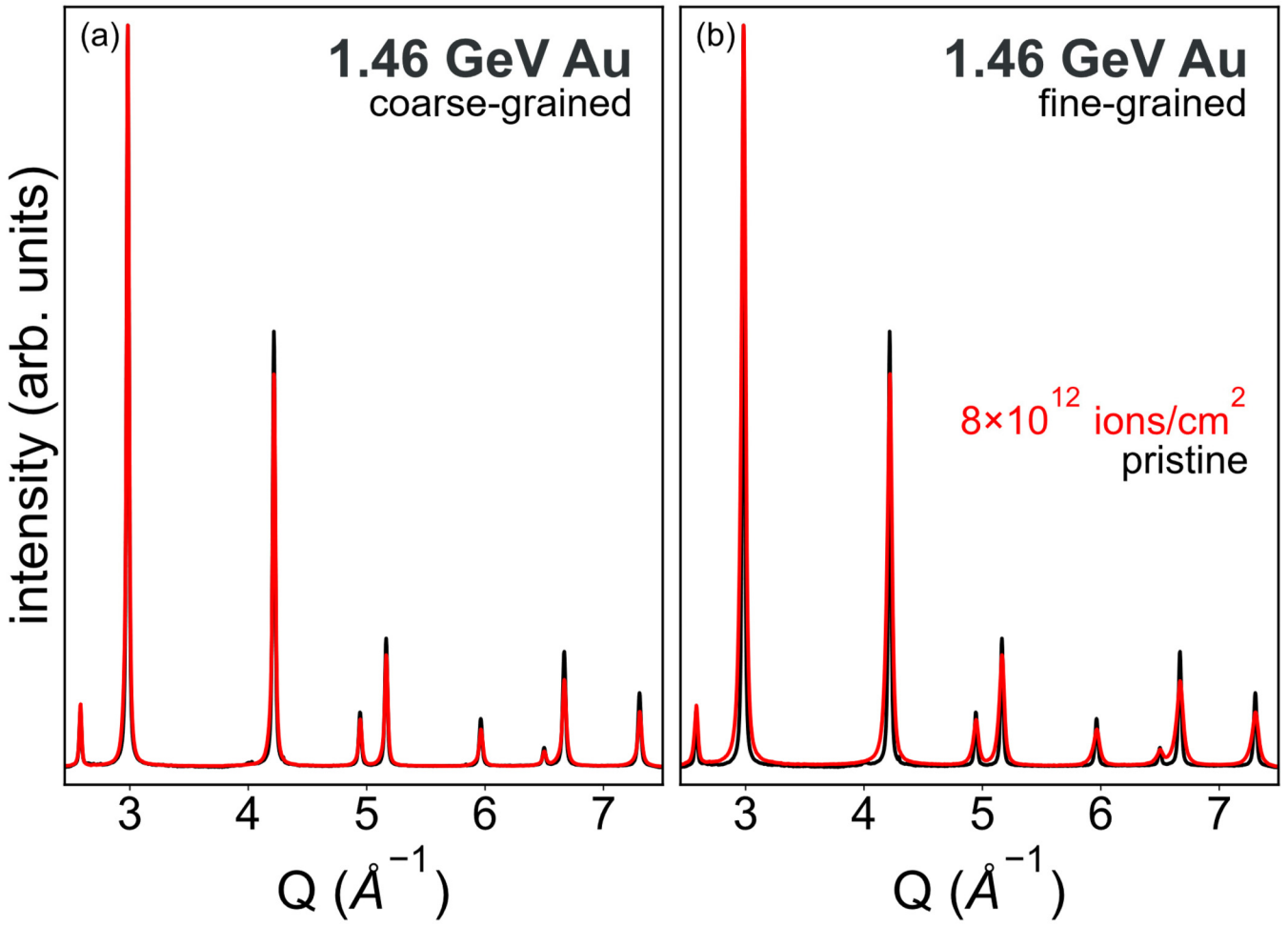

FIG. 6. X-ray diffraction patterns of (a) coarse- and (b) fine-grained MgO before and after exposure to 8×10^{12} 1.46 GeV Au ions/cm^2.

quantify a narrow region in S_n/S_e that leads to appreciable electronic-dominated defects (Fig. 10).

Our high-throughput irradiation approach for two ion conditions (198 MeV Xe and 946 MeV Au) enabled XRD analysis of MgO over a broad fluence range, capturing both the magnitude and fluence dependence of unit-cell expansion. At low fluences, lattice swelling increases proportionally with ion exposure, consistent with defect accumulation. At higher fluences, defect creation and recovery enter a steady-state regime, leading to saturation in unit-cell expansion. This behavior, observed in many irradiated insulators such as CeO_2,[65–68] reflects a direct impact mechanism.[60] For MgO, the saturation lattice swelling under high-energy, highly ionizing conditions remains below 0.1%, similar to other simple oxides.[69] Fitting the direct impact model to our lattice swelling data yields damage diameters of 4.9(2) nm and 4.7(4) nm for coarse- and fine-grained MgO, respectively. These values are comparable to those reported for CeO_2 and ThO_2 under 167 MeV Xe irradiation, where synchrotron XRD analysis revealed damage diameters of 3.9 (3) nm and 3.0(1) nm, respectively.[69]

Unlike the clear fluence-dependent lattice swelling observed for 198 MeV Xe irradiation, MgO samples exposed to 946 MeV Au ions exhibit more complex behavior. The coarse-grained sample experienced modest unit-cell expansion to approximately 0.02% at the lowest fluence tested, with no clear trend at higher fluences. In contrast, the fine-grained sample initially contracted, a rare response for oxides under swift heavy ion irradiation. This initial contraction may reflect the annealing of pre-existing defects, potentially related to the smaller grain size or synthesis conditions. This interpretation is supported by the slightly larger unit cell observed in the fine-grained sample before irradiation. At higher fluences, unit-cell expansion is observed, suggesting defect accumulation. Alternatively, the fine-grained sample may follow a two-stage response to irradiation. Similar behavior has been reported in monocarbides such as ZrC and HfC under 946 MeV Au

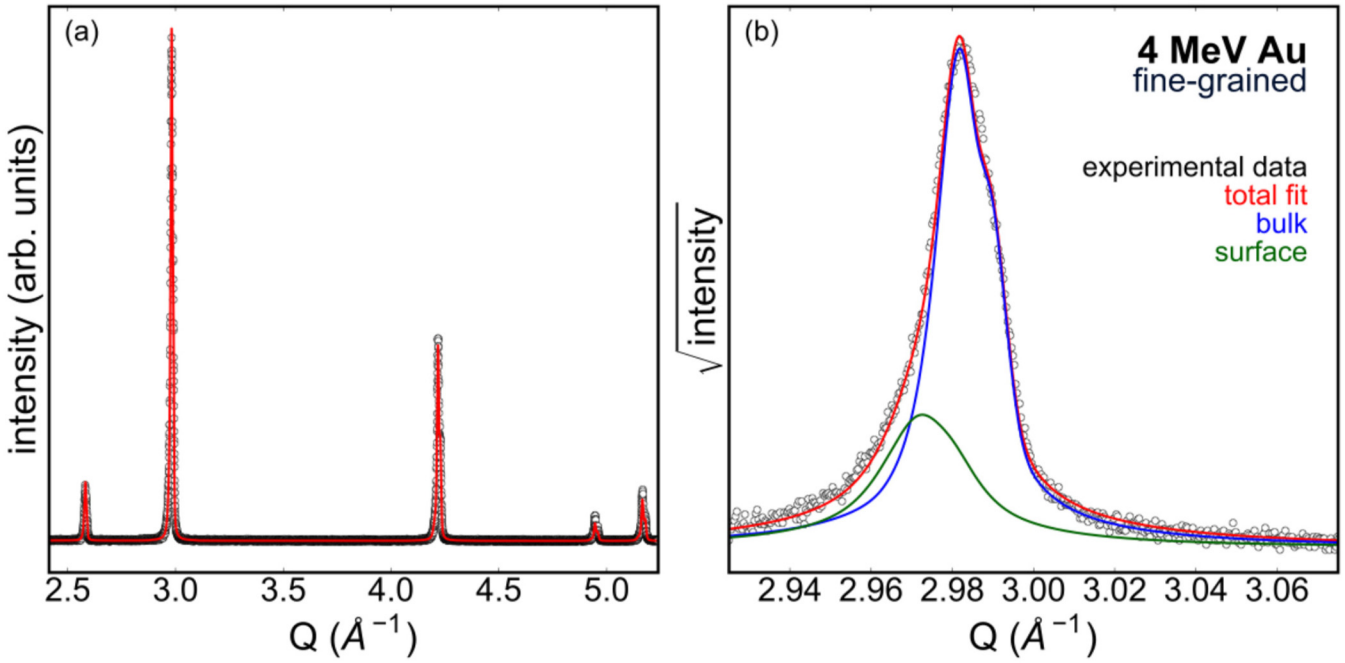

FIG. 7. GIXRD pattern for fine-grained MgO exposed to 4 MeV Au to a fluence of 7.8×10^{15} ions/cm^2. Panel (a) shows the full pattern with experimental data (black dots) and refinement (red solid line), while (b) delineates the different components for the (200) peak including the bulk (blue solid line) and surface (green solid line).

irradiation,[48,70] where an initial direct impact-like expansion is followed by a linear increase beyond fluences of $1–2 \times 10^{13}$ ions/cm^2, a range consistent with our data. A third possibility involves surface-specific and grain boundary effects.[63,64] The high grain boundary density in the fine-grained material potentially provides a network of efficient sinks for mobile point defects. Under these conditions, irradiation initially promotes the removal of pre-existing defects and residual strain introduced through processing, resulting in a lattice compaction. This effect is expected to be less pronounced in coarse-grained MgO, where the lower grain boundary area reduces sink efficiency and limits defect annihilation.

The consistent observation of unit-cell expansion under all irradiation conditions confirms that both nuclear and electronic interactions induce defects in MgO. However, unit-cell swelling reflects long-range, homogeneous structural changes, while the same defects may also cause short-range, localized distortions. These localized distortions introduce heterogeneity in interplanar spacing, manifesting as peak broadening rather than peak shifts in XRD patterns. As peak broadening can also result from reduced coherent domain size, the W–H analysis was conducted to disentangle size and strain effects. Interestingly, under 946 MeV Au irradiation, the unit-cell expansion in MgO does not follow a direct impact behavior, whereas the microstrain accumulation does. The inverse is observed for 198 MeV Xe irradiation: lattice swelling follows direct impact behavior, but microstrain does not. This contrast may indicate that under irradiation conditions where nuclear energy deposition is minimal (e.g., 946 MeV Au), the resulting defects are more dilute and contribute primarily to localized distortions, leading to elevated strain but minimal volumetric expansion. In contrast, conditions with a higher contribution from nuclear interactions (e.g., 198 MeV Xe) may produce more uniformly distributed damage, resulting in greater lattice swelling but less accumulated strain. This interpretation is supported by the analysis in Fig. 10, which like Fig. 9(b), relates maximum microstrain to the partitioning of energy loss. The microstrain increase in MgO under 946 MeV Au irradiation is approximately an order of magnitude greater than that observed under 198 MeV Xe and 4 MeV Au conditions, both of which show only modest strain increases. For 1.46 GeV Au irradiation, the microstrain increase is also lower—possibly due to its reduced nuclear energy loss, the lower energy density from higher ion velocities, and/or the limited single-fluence data point (8×10^{12} ions/cm^2), which may not capture the full saturation behavior.

The most pronounced lattice swelling observed in this study occurred under irradiation conditions dominated by nuclear energy loss, consistent with the expectation that displacement cascades promote the formation and growth of extended defect structures such as vacancy and interstitial loops.[25,26] This observation aligns with prior work linking nuclear stopping to defect clustering and long-range volumetric expansion in oxides. In contrast, irradiation conditions characterized by higher electronic stopping led to comparatively smaller increases in unit-cell size but greater accumulation of microstrain. This may reflect a defect population dominated

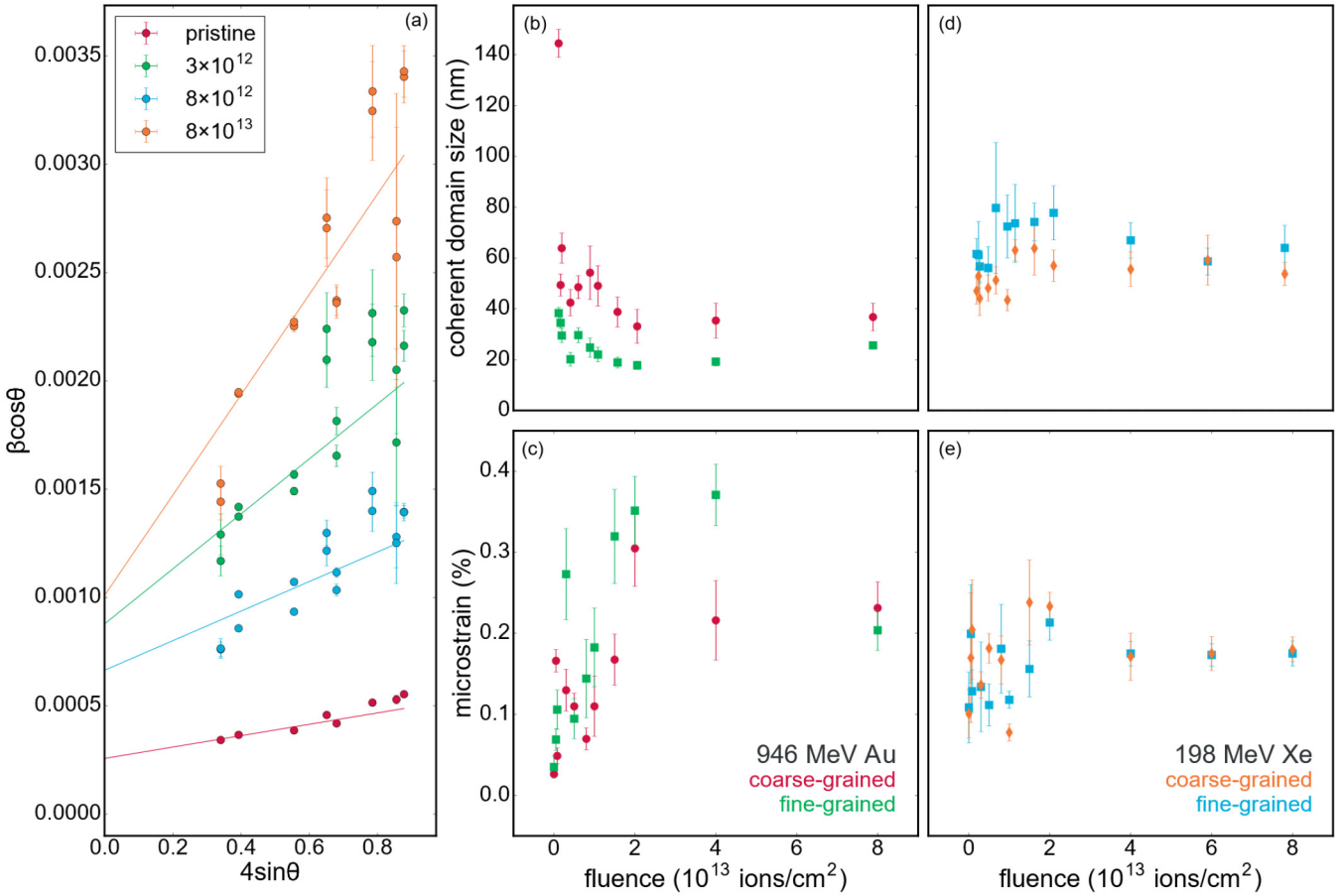

FIG. 8. (a) Representative Williamson–Hall analysis of coarse-grained MgO samples before and after exposure to indexed fluences of 946 MeV Au ions. The intercept and slope of lines in (a) are used to determine the [(b) and (d)] coherent domain size and [(c) and (e)] heterogeneous microstrain, respectively. Data in (b) and (c) correspond to 946 MeV Au irradiation, while (d) and (e) correspond to 198 MeV Xe irradiation. Uncertainties in (a) arise from peak fitting of the XRD patterns and are propagated to uncertainties in [(b) and (c)] and [(d) and (e)], which also incorporate uncertainties from the linear regressions shown in (a).

TABLE II. Summary of the maximum observable lattice swelling identified, through Rietveld refinement of x-ray diffraction patterns, in all irradiated MgO samples.

Ion irradiation conditions	MgO specimen	Maximum fluence (ions/cm^2)	Maximum lattice swelling (%)
4 MeV Au	Fine-grained	7.8×10^{15}	0.3640(3)
		4.0×10^{15}	0.3773(4)
198 MeV Xe	Fine-grained	8×10^{13}	0.0797(4)
	Coarse-grained	8×10^{13}	0.0705(4)
946 MeV Au	Fine-grained	8×10^{13}	0.0618(4)
	Coarse-grained	8×10^{13}	0.0376(11)
1.46 GeV Au	Fine-grained	8×10^{13}	0.0041(1)
	Coarse-grained	8×10^{13}	0.0081(5)

by isolated Frenkel pairs or point-like disorder, where high-density energy deposition causes localized distortions but does not efficiently drive defect aggregation. Moreover, the more diffuse nature of electronic energy deposition may suppress dynamic annealing, enabling strain to persist. Together, these results suggest a divergence in how nuclear and electronic stopping mechanisms influence structural modification in MgO: nuclear interactions appear to promote lattice swelling through defect coalescence and long-range distortion, whereas electronic interactions predominantly induce microstrain via short-range, localized damage. While both regimes produce defects, the spatial distribution, recovery dynamics, and aggregation behavior differ, contributing to the distinct structural responses observed across the irradiation conditions.

While aspects of the fluence dependence observed in this work resemble phenomenology often described using direct impact

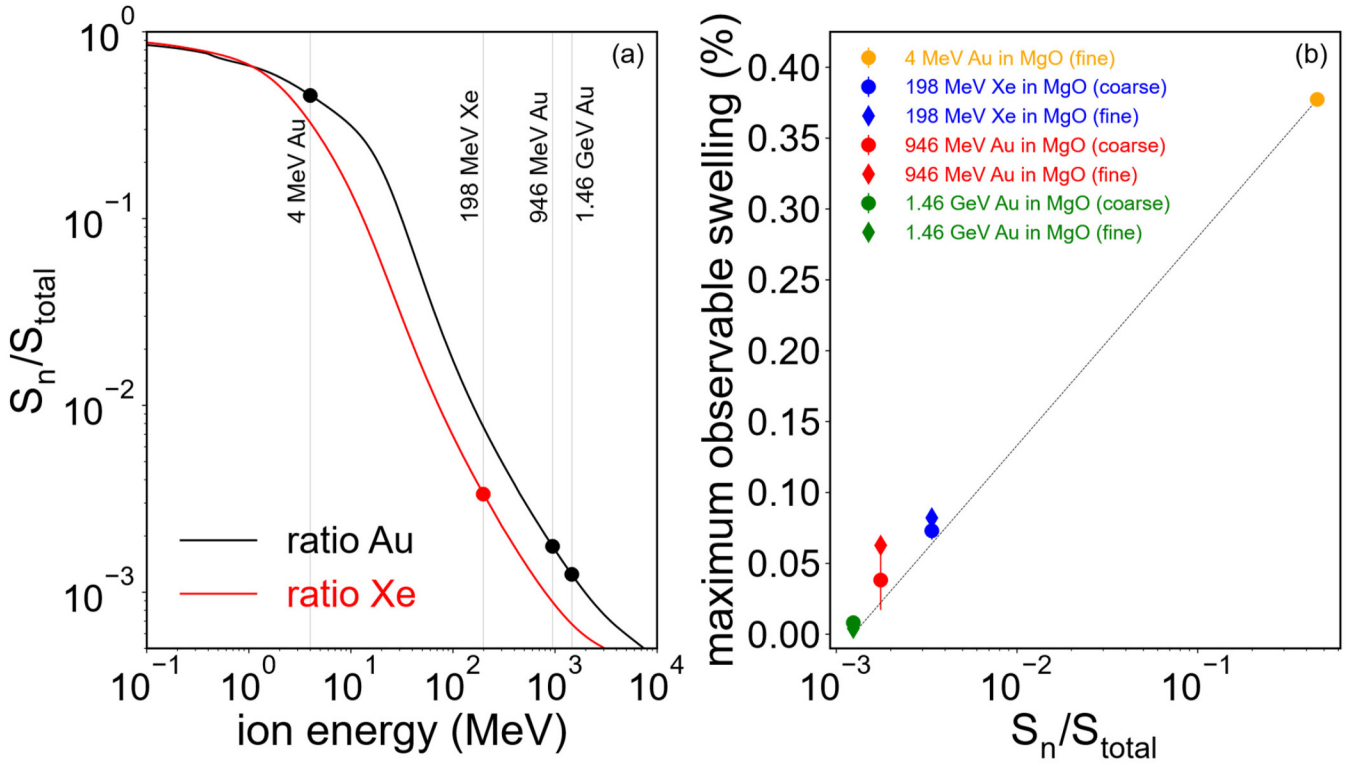

FIG. 9. (a) Fraction of ion energy loss arising from nuclear interactions as a function of ion energy for Au and Xe ions. The four ions chosen for this study are denoted by black (Au) or red (Xe) dots. (b) The maximum observable lattice swelling, as extracted from XRD analysis, presented against the ratio from (a). The gray lines are shown to guide the eye.

or cascade overlap terminology, it is important to note that MgO does not form stable ion tracks. Numerous experimental and modeling studies have shown that interstitials in MgO exhibit high mobility even at room temperature, enabling rapid recombination with vacancies, migration to sinks, and the formation of extended defect structures such as dislocation loops rather than persistent cascade remnants. Consequently, the physical meaning of cascade overlap in MgO differs substantially from that in materials where tracks or amorphous zones are stable. In this context, the evolution of lattice expansion, microstrain, and coherent domain size observed here can be interpreted within a defect production–migration–accumulation framework. Such approaches explicitly account for the balance between defect generation, recombination, clustering, and annihilation at sinks, and have been applied to MgO over a wide range of temperatures and irradiation conditions.

Debelle *et al.*[71] demonstrated that the fluence dependence of defect accumulation in MgO can be explained by defect mobility-controlled kinetics, without invoking persistent damage zones or track overlap, and highlighted the central role of migration rates in determining steady-state behavior. Earlier experimental work by Kinoshita[31] similarly emphasized the high mobility of defects in MgO and reported the formation of extended defects such as dislocation loops even at irradiation temperatures near 300 K, underscoring the dynamic nature of defect evolution in this material. The apparent saturation in the microstrain and lattice expansion quantified here after high fluences does not uniquely imply a direct impact or cascade overlap mechanism but may instead reflect a steady state in which defect production is balanced by recovery processes governed by defect migration and sink interactions where dose rate effects are negligible. Differences between the nuclear- and electronic-stopping-dominated irradiations can thus be understood in terms of defect production bias and spatial correlation, consistent with models in which clustered defect production in displacement cascades leads to larger, longer-range strain fields than the more diffuse defect generation associated with electronic energy loss. This interpretation is aligned with the production bias concept introduced by Woo and Singh,[72] while remaining fully compatible with the high interstitial mobility in MgO. Accordingly, the use of direct impact terminology in this work should be viewed as a phenomenological description of the observed accumulation behavior rather than as evidence for the formation of stable ion tracks. The XRD results are equally consistent with a defect accumulation picture, where the irradiation response is controlled by the interplay between defect generation rates, migration kinetics, and microstructural sinks.

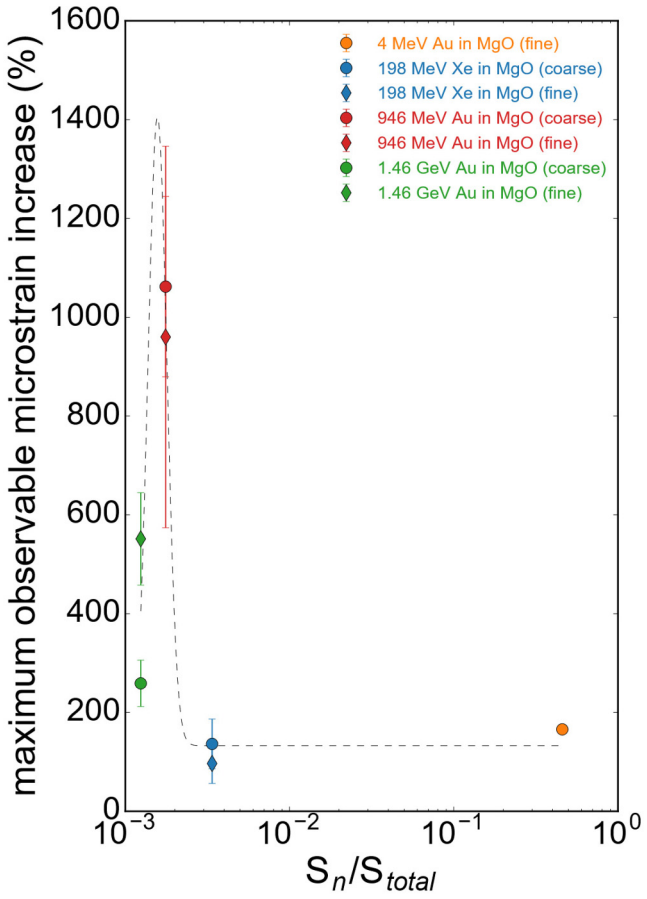

FIG. 10. Maximum observable microstrain increase, as extracted from XRD pattern analysis, presented against the ratio from Fig. 9(a). The gray dashed line is shown to guide the eye.

V. CONCLUSIONS

X-ray analysis revealed consistent unit-cell expansion in MgO across a range of ion irradiation conditions: 4 MeV Au (dominated by nuclear stopping), and 198 MeV Xe, 946 MeV Au, and 1.46 GeV Au (dominated by electronic excitations). The most pronounced lattice swelling was observed after exposure to low-energy 4 MeV Au ions, while high-energy 1.46 GeV Au irradiation-induced minimal expansion, differing by nearly two orders of magnitude. This inverse relationship between lattice swelling magnitude and ion energy suggests that displacive, knock-on damage is significantly more effective at inducing volumetric changes than ionization-driven processes. Moreover, under highly ionizing conditions, the extent and nature of damage appear to depend on the spatial distribution of energy deposition. Higher energy density conditions (such as 198 MeV Xe) lead to more homogeneous, long-range distortion manifesting as unit-cell expansion, whereas lower energy density conditions (such as 946 MeV and 1.46 GeV Au) result in more localized damage, reflected in increased microstrain. These findings provide critical insight into the mechanisms by which radiation modifies MgO, highlighting the distinct structural responses induced by nuclear vs electronic interactions. The results serve as a valuable benchmark for understanding radiation effects in simple oxides and informing the design of radiation-tolerant materials for advanced nuclear energy systems and the broader nuclear fuel cycle.

ACKNOWLEDGMENTS

This work was funded by the U.S. Department of Energy Advanced Research Projects Agency-Energy (ARPA-E) ONWARDS Program under Award No. DE-AR0001620. The results are based on a UMAT experiment performed the UNILAC at the GSI Helmholtzzentrum für Schwerionenforschung, Darmstadt (Germany), within the framework of FAIR Phase-0. XRD measurements were conducted at HPCAT (Sector 16), Advanced Photon Source (APS), Argonne National Laboratory. HPCAT is supported by the DOE-NNSA's Office of Experimental Sciences. APS is a U.S. Department of Energy (DOE) Office of Science User Facility operated by Argonne National Laboratory under Contract No. DE-AC02-06CH11357. This research used the X-ray powder diffraction beamline of the National Synchrotron Light Source II, a U.S. DOE Office of Science User Facility operated for the DOE Office of Science by Brookhaven National Laboratory under Contract No. DE-SC0012704. The views and opinions of authors expressed herein do not necessarily state or reflect those of the United States Government or any agency thereof.

AUTHOR DECLARATIONS

Conflict of Interest

The authors have no conflicts to disclose.

Author Contributions

Eric C. O'Quinn: Data curation (equal); Formal analysis (equal); Investigation (equal); Methodology (supporting); Validation (equal); Visualization (equal); Writing – original draft (lead); Writing – review & editing (supporting). **David J. Sprouster:** Data curation (equal); Formal analysis (equal); Investigation (equal); Visualization (equal); Writing – original draft (equal); Writing – review & editing (supporting). **Cale C. Overstreet:** Formal analysis (supporting); Visualization (supporting). **Jacob Minnette:** Formal analysis (supporting); Visualization (supporting). **M. Saima Haque:** Data curation (supporting); Formal analysis (supporting); Investigation (supporting); Visualization (supporting). **Maria Eugenia Toimil-Molares:** Investigation (supporting); Resources (equal). **Miguel L. Crespillo:** Investigation (supporting); Resources (equal). **Maik K. Lang:** Conceptualization (equal); Funding acquisition (equal); Investigation (supporting); Methodology (equal); Supervision (equal); Writing – original draft (supporting); Writing – review & editing (supporting). **Lance L. Snead:** Conceptualization (supporting); Writing – review & editing (supporting). **Jason R. Trelewicz:** Conceptualization (lead); Funding acquisition (lead); Methodology (equal); Project administration (equal); Supervision (equal); Writing – original draft (supporting); Writing – review & editing (lead).

DATA AVAILABILITY

The data that support the findings of this study are available from the corresponding author upon reasonable request.

REFERENCES

[1]J. A. L. Robertson, A. M. Ross, M. J. F. Notely, and J. R. MacEwan, J. Nucl. Mater. **7**, 225–262 (1962).
[2]A. F. Fuentes, E. C. O'Quinn, S. M. Montemayor, H. Zhou, M. Lang, and R. C. Ewing, Appl. Phys. Rev. **11**, 1–140 (2024).
[3]R. C. Ewing, Proc. Natl. Acad. Sci. U.S.A. **96**, 3432–3439 (1999).
[4]L. Thomé, S. Moll, A. Debelle, F. Garrido, G. Sattonnay, and J. Jagielski, Adv. Mater. Sci. Eng. **2012**, 905474.
[5]C. L. Tracy, M. Lang, F. Zhang, S. Park, R. I. Palomares, and R. C. Ewing, Prog. Nucl. Energy **104**, 342–358 (2018).
[6]*Uncertainty Underground: Yucca Mountain and the Nation's High-Level Nuclear Waste*, edited by A. Macfarlane and R. C. Ewing (MIT Press, 2006).
[7]R. C. Ewing, W. J. Weber, and J. Lian, J. Appl. Phys. **95**, 5949–5971 (2004).
[8]L. W. Hobbs, F. W. Clinard, S. J. Zinkle, and R. C. Ewing, J. Nucl. Mater. **216**, 291–321 (1994).
[9]A. V. Lankin, I. V. Morozov, G. E. Norman, S. A. Pikuz, and I. Y. Skobelev, Phys. Rev. E: Stat., Nonlinear, Soft Matter Phys. **793**, 036407 (2009).
[10]N. Medvedev, A. E. Volkov, R. Rymzhanov, F. Akhmetov, S. Gorbunov, R. Voronkov, and P. Babaev, J. Appl. Phys. **133**, 100701 (2023).
[11]A. Benyagoub, Phys. Rev. B **72**, 21–24 (2005).
[12]P. Kluth, C. S. Schnohr, O. H. Pakarinen, F. Djurabekova, D. J. Sprouster, R. Giulian, M. C. Ridgway, A. P. Byrne, C. Trautmann, D. J. Cookson, K. Nordlund, and M. Toulemonde, Phys. Rev. Lett. **101**, 1–4 (2008).
[13]S. J. Zinkle, Nucl. Instrum. Methods Phys. Res., Sect. B **91**, 234–246 (1994).
[14]Y. Chen and W. A. Sibley, Phys. Rev. **154**, 842–850 (1967).
[15]A. J. Tench and M. J. Duck, J. Phys. C: Solid State Phys. **6**, 1134 (1973).
[16]W. A. Sibley and Y. Chen, Phys. Rev. **160**, 712–716 (1967).
[17]J. E. Wertz, P. Auzins, R. A. Weeks, and R. H. Silsbee, Phys. Rev. **107**, 1535–1537 (1957).
[18]B. P. Uberuaga, R. Smith, A. R. Cleave, G. Henkelman, R. W. Grimes, A. F. Voter, and K. E. Sickafus, Phys. Rev. B **71**, 1–12 (2005).
[19]L. L. Snead, D. Sprouster, B. Cheng, N. Brown, C. Ang, E. M. Duchnowski, X. Hu, and J. Trelewicz, J. Asian Ceram. Soc. **10**, 9–32 (2022).
[20]G. F. Hurley, J. C. Kennedy, F. W. Clinard, R. A. Youngman, and W. R. McDonell, J. Nucl. Mater. **103**, 761–765 (1981).
[21]E. T. Cheng and G. R. Hopkins, Nuclear Technology/Fusion, AA (General Atomics, California), AB(General Atomics, California), 4(2), 701–706 (1983).
[22]S. J. Zinkle and L. L. Snead, Nucl. Instrum. Methods Phys. Res., Sect. B **116**, 92–101 (1996).
[23]D. Bhardwaj, B. Cheng, D. J. Sprouster, W. S. Cunningham, N. Rani, J. R. Trelewicz, and L. L. Snead, Front. Nucl. Eng. **3**, 1–12 (2024).
[24]J. W. Fletcher, E. E. Peterson, J. R. Trelewicz, and L. L. Snead, Fusion Sci. Technol. 1–16 (2025).
[25]G. W. Groves and A. Kelly, Philos. Mag. **6**, 1527 (1961).
[26]D. H. Bowen, R. S. Wilks, and F. J. P. Clarke, J. Nucl. Mater. **6**, 148–151 (1962).
[27]L. M. Wang, S. X. Wang, W. L. Gong, R. C. Ewing, and W. J. Weber, Mater. Sci. Eng. A **253**, 106–113 (1998).
[28]K. Trachenko, M. T. Dove, E. Artacho, I. T. Todorov, and W. Smith, Phys. Rev. B **73**, 174207 (2006).
[29]S. X. Wang, L. M. Wang, R. C. Ewing, and R. H. Doremus, J. Non-Cryst. Solids **238**, 214–224 (1998).
[30]F. W. Clinard, G. F. Hurley, and L. W. Hobbs, J. Nucl. Mater. **108–109**, 655–670 (1982).
[31]C. Kinoshita, K. Hayashi, and S. Kitajima, Nucl. Instrum. Methods Phys. Res., Sect. B **1**, 209–218 (1984).
[32]N. Itoh, D. M. Duffy, S. Khakshouri, and A. M. Stoneham, J. Phys. Condens. Matter **21**, 474205–474214 (2009).
[33]A. L. Shluger, R. W. Grimes, C. R. A. Catlow, and N. Itoh, J. Phys.: Condens. Matter **3**, 8027–8036 (1991).
[34]T. Katsumi and I. Noriaki, Nucl. Instrum. Methods Phys. Res., Sect. B **46**, 207–215 (1990).
[35]A. M. Stoneham, Nucl. Instrum. Methods Phys. Res., Sect. B **91**, 1–11 (1994).
[36]R. I. Palomares, J. Shamblin, C. L. Tracy, J. Neuefeind, R. C. Ewing, C. Trautmann, and M. Lang, J. Mater. Chem. A **5**, 12193–12201 (2017).
[37]D. Peak, J. W. Corbett, and J. C. Bourgoin, J. Chem. Phys. **65**, 1206–1210 (1976).
[38]S. J. Zinkle, V. A. Skuratov, and D. T. Hoelzer, Nucl. Instrum. Methods Phys. Res., Sect. B **191**, 758–766 (2002).
[39]J. C. Bourgoin and J. W. Corbett, Phys. Lett. A **38**, 135–137 (1972).
[40]M. Beauvy, C. Dalmasso, C. Thiriet-Dodane, D. Simeone, and D. Gosset, Nucl. Instrum. Methods Phys. Res., Sect. B **242**, 557–561 (2006).
[41]S. Moll, Y. Zhang, A. Debelle, L. Thomé, J. P. Crocombette, Z. Zihua, J. Jagielski, and W. J. Weber, Acta Mater. **88**, 314–322 (2015).
[42]G. Coiana, J. Lischner, and P. Tangney, Phys. Rev. B **109**, 14310 (2024).
[43]D. J. Sprouster, L. Gurnani, M. Ouyang, K. Christian, B. Cheng, W. S. Cunningham, P. Negi, S. K. Ghose, Y. Zheng, D. J. Hwang, M. M. Karatas, S. J. Zinkle, J. R. Trelewicz, and L. L. Snead, J. Eur. Ceram. Soc. **46**(5), 118043 (2026).
[44]B. Cheng, E. M. Duchnowski, D. J. Sprouster, L. L. Snead, N. R. Brown, and J. R. Trelewicz, J. Nucl. Mater. **563**, 153591 (2022).
[45]E. C. O'Quinn, J. M. Hirtz, C. C. Overstreet, W. F. Cureton, I. M. Gussev, A. P. Solomon, M. E. Toimil-Molares, and M. K. Lang, Nucl. Sci. Eng. 1–15 (2025).
[46]J. F. Ziegler, M. D. Ziegler, and J. P. Biersack, Nucl. Instrum. Methods Phys. Res., Sect. B **268**, 1818–1823 (2010).
[47]W. F. Cureton, R. I. Palomares, J. Walters, C. L. Tracy, C. H. Chen, R. C. Ewing, G. Baldinozzi, J. Lian, C. Trautmann, and M. Lang, Acta Mater. **160**, 47–56 (2018).
[48]J. Minnette, E. Williams, William Cureton, A. Solomon, E. O'Quinn, M. Kurley, R. D. Hunt, C. Park, I. Schubert, C. Trautmann, and M. Lang, J. Appl. Phys. **134**, 185901 (2023).
[49]J. Shamblin, C. L. Tracy, R. C. Ewing, F. Zhang, W. Li, C. Trautmann, and M. Lang, Acta Mater. **117**, 207–215 (2016).
[50]C. Prescher and V. B. Prakapenka, High Pressure Res. **35**, 223–230 (2015).
[51]O. Ivashkevych *et al.*, "Hard x-ray pair distribution function (PDF) beamline and end-station control system," in Proc. ICALEPCS'19 (New York, 2019), pp. 1584–1589.
[52]B. H. Toby and R. B. Von Dreele, J. Appl. Crystallogr. **46**, 544–549 (2013).
[53]D. Balzar, N. Audebrand, M. R. Daymond, A. Fitch, A. Hewat, J. I. Langford, A. L. Bail, D. Louër, O. Masson, C. N. McCowan, N. C. Popa, P. W. Stephens, and B. H. Toby, J. Appl. Crystallogr. **37**, 911–924 (2004).
[54]M. Wojdyr, J. Appl. Crystallogr. **43**, 1126–1128 (2010).
[55]T. Ungár, Scr. Mater. **51**(8), 777–781 (2004).
[56]D. J. Sprouster, T. Koyanagi, E. Dooryhee, S. K. Ghose, Y. Katoh, and L. E. Ecker, Scr. Mater. **143**, 176–180 (2018).
[57]G. K. Williamson and W. H. Hall, Acta Metall. **1**, 22–31 (1953).
[58]W. L. Bragg, Nature **105**, 646–648 (1920).
[59]S. Sasaki, Y. Takeuchi, and K. Fujino, Proc. Jpn. Acad., Ser. B **55**, 43–48 (1979).
[60]J. F. F. Gibbons, Proc. IEEE **60**, 1062–1096 (1972).
[61]A. Meftah, F. Brisard, J. M. Costantini, M. Hage-Ali, J. P. Stoquert, F. Studer, and M. Toulemonde, Phys. Rev. B **48**, 920–925 (1993).

[62]A. Kamarou, W. Wesch, E. Wendler, A. Undisz, and M. Rettenmayr, Phys. Rev. B **73**, 1–16 (2006).
[63]X.-M. Bai and B. P. Uberuaga, JOM **65**(3), 360–373 (2013).
[64]I. J. Beyerlein, M. J. Demkowicz, A. Misra, and B. P. Uberuaga, Prog. Mater. Sci. **74**, 125–210 (2015).
[65]C. L. Tracy, J. Shamblin, S. Park, F. Zhang, C. Trautmann, M. Lang, and R. C. Ewing, Phys. Rev. B **94**, 1–11 (2016).
[66]M. Lang, F. Zhang, J. Zhang, J. Wang, J. Lian, W. J. Weber, B. Schuster, C. Trautmann, R. Neumann, and R. C. Ewing, Nucl. Instrum. Methods Phys. Res., Sect. B **268**, 2951–2959 (2010).
[67]G. Sattonnay, C. Grygiel, I. Monnet, C. Legros, M. Herbst-Ghysel, and L. Thomé, Acta Mater. **60**, 22–34 (2012).
[68]J. Jagielski and L. Thomé, Vacuum **81**, 1352–1356 (2007).
[69]C. L. Tracy, M. Lang, J. M. Pray, F. Zhang, D. Popov, C. Park, C. Trautmann, M. Bender, D. Severin, V. A. Skuratov, and R. C. Ewing, Nat. Commun. **6**, 6133 (2015).
[70]E. Williams, J. Minnette, E. O'Quinn, A. Solomon, C. Overstreet, W. F. Cureton, I. Schubert, C. Trautman, C. Park, M. Zdorovets, and M. Lang, Nucl. Instrum. Methods Phys. Res., Sect. B **548**, 165248 (2024).
[71]A. Debelle, J.-P. Crocombette, A. Boulle, E. Martinez, B. P. Uberuaga, D. Bachiller-Perea, Y. Haddad, F. Garrido, L. Thomé, and M. Béhar, Phys. Rev. Mater. **2**(8), 083605 (2018).
[72]C. H. Woo and B. N. Singh, Philos. Mag. A **65**(4), 889–912 (1992).